Magnetic Phase Crossover in strongly correlated $EuMn_2P_2$

Tanya Berry[†,‡*], Nicodemos Varnava[§], Dominic Ryan[¶], Veronica Stewart[†,‡], Riho Rästa[#], Ivo Heinmaa[#], Nitesh Kumar[††], Walter Schnelle[††], Rishi Bhandia[‡], Christopher Pasco[†,‡], N.P. Armitage[‡], Raivo Stern[#], Claudia Felser[††], David Vanderbilt[§], Tyrel M. McQueen[†,‡,‡‡]

† Department of Chemistry, The Johns Hopkins University, Baltimore, Maryland 21218, USA

‡ Institute for Quantum Matter, William H. Miller III Department of Physics and Astronomy, The Johns Hopkins University, Baltimore, Maryland 21218, USA

§ Department of Physics & Astronomy, Rutgers University, Piscataway, NJ 08854, USA

¶ Physics Department and Centre for the Physics of Materials, McGill University, 3600 University Street, Montreal, Quebec, H3A 2T8, Canada

National Institute of Chemical Physics and Biophysics, Akadeemia tee 23, 12618 Tallinn, Estonia

†† Max-Planck-Institute for Chemical Physics of Solids, D-01187 Dresden, Germany

‡‡ Department of Materials Science and Engineering, The Johns Hopkins University, Baltimore, Maryland 21218, USA

*Corresponding author email: tberry@ucdavis.edu

CONTENTS

MATERIALS AND METHODS:

Single Crystal Growth and Diffraction: The single crystals of $EuMn_2P_2$ were grown via Sn flux method as previously reported.[1] The single crystals had a hexagonal plate like morphology, 0.5–2 mm in width. Powder X-ray diffraction and X-ray energy dispersive spectroscopy (EDS) were used to confirm the phase purity and elemental composition of the single crystals. Single crystal X-ray diffraction data were collected using a SuperNova diffractometer equipped with an Atlas detector and a Mo Kα source. The cuboid crystal, cut from a larger crystal piece, was mounted with Paratone-N oil. Data was analyzed and reduced using the CrysAlisPro software suite, version 1.171.36.32 (2013), Agilent Technologies. Initial structural models were developed using SIR92 and refinements of this model were done using SHELXL-97 (WinGX version, release 97-2).[2,3] Real-time back reflection Laue X-ray diffraction was used to orient and align the crystals for measurement. Single crystals of $EuZn_2P_2$ for phonon subtractions were also synthesized using a Sn flux, via a similar method that will be reported elsewhere. The single crystals of $EuZn_2P_2$ and $EuMn_2P_2$ were found to be stable on the benchtop.

DFT Calculations: The bulk of the first-principle calculations were performed using the Vienna abinitio simulation package (VASP), and the GGA with the Perdew−Burke−Ernzerhof (PBE) type exchange correlation potential was adopted. For the self-consistent calculations a Monkhorst-Pack k-mesh of size 14 × 14 × 4 was used to sample the Brillouin zone (BZ). The energy cutoff is chosen 1.5 times as large as the values recommended in relevant pseudopotentials. Spin-orbit coupling (SOC) was included self-consistently as described in the text. The Eu 4f states were treated by employing the GGA+U approach with the U value set to 5.0eV. A Hubbard U = 5 eV for Mn was used where described in the text.

Optical Spectroscopy: Transmissivity of $EuMn_2P_2$ single crystals was measured using a commercial FTIR spectrometer (Bruker Vertex 80V, Source: Globar, Detector: MCT) in the MIR (400 cm^{-1} to 6000 cm^{-1}) at room temperature. The complex conductivity of the material was determined using Kramers-Kronig (KK) constrained variational dielectric function (VDF) fitting as implemented in the freely available software RefFit.[4] This fitting method is an alternative to the traditional approach of using a KK transform to determine the complex conductivity.

Bulk Magnetic Properties Measurements: Magnetization measurements were performed in a vibrating sample superconducting quantum interference device magnetometer (SQUID-VSM) from Quantum Design. All measurements were carried out after cooling in zero field. To reduce the remnant field of the superconducting magnet to less than 2 Oe before each measurement, we applied a magnetic field of 5 T at ambient temperature and then removed it in an oscillation mode. The magnetic field was applied parallel and perpendicular to the rod crystal direction of the single crystals that corresponds to the c-axis. Sample shape correction was accounted for in these measurements. In addition to the standard magnetization as a function of field and temperature, the oven option was used to measure the magnetization at high temperatures T=300-700K. The sample was mounted using the Zircar Cement for the oven option.

The Curie-Weiss law:

$$\chi(T) = \chi_0 + \frac{C}{T-\theta_{CW}} \quad (1)$$

where χ_0 is the temperature-independent susceptibility, C is the Curie constant, and θ_{CW} is the Weiss temperature, was used to analyze the high temperature behavior.

Thermodynamic and Electrical Transport Properties: All of the thermodynamic and electrical transport properties measurements were carried out in the Physical Properties Measurement System (PPMS-9), Quantum Design. The heat capacity measurements on the single crystals of $EuMn_2P_2$ and $EuZn_2P_2$ was collected from T = 2-300 K under applied fields of $\mu_o H$=0.1T. These measurements utilized the heat

capacity option in the PPMS-9 using the semi-adiabatic pulse technique with a 1% temperature rise and three repetitions at each temperature.

The resistivity option in the PPMS-9 was utilized to carry out the resistivity measurements. The resistivity was measured from T = 200-400 K using the four-probe technique. The leads were made out of Pt wire and the contacts were made using Dupont 4922N Ag paste. The Pt lead distance was 0.38 mm. The sample length was 1.3 mm longitudinally. The Hall resistivity data were antisymmetrized with respect to the applied magnetic field whereas the longitudinal resistivity data were symmetrized. For the temperature-dependent where T=300K, two temperature sweeps were carried out, one with a positive and one with a negative field of the same magnitude. The data were subsequently antisymmetrized to subtract the contribution of the longitudinal resistivity.

$$\rho_{xx}(\mu_o H) = \frac{\rho(+\mu_o H)+\rho(-\mu_o H)}{2} \tag{2}$$

$$\rho_{xy}(\mu_o H) = \frac{\rho(+\mu_o H)-\rho(-\mu_o H)}{2}\left(\frac{L}{w}\right) \tag{3}$$

Where $\rho(+\mu_o H)$, $\rho(-\mu_o H)$ indicate the measured resistivity at positive and negative values of the magnetic field, respectively, while *L* and *W* designates the length and the width of the sample.

The phonons for $EuZn_2P_2$ were subtracted by first constructing an equivalent Debye model and then scaling for the small molecular mass difference between Zn and Mn. The two Debye model used is:

$$\frac{C_p}{T} = \frac{C_D(\theta_{D1},s_1,T)}{T} + \frac{C_D(\theta_{D2},s_2,T)}{T} \tag{4}$$

$$\mathrm{C_D}(\theta_\mathrm{D},\mathrm{T}) = 9sR\left(\frac{\mathrm{T}}{\theta_\mathrm{D}}\right)^3 \int_0^{\theta_\mathrm{D}/\mathrm{T}} \frac{(\theta/\mathrm{T})^4 e^{\theta/\mathrm{T}}}{[e^{\theta/\mathrm{T}}-1]^2}\,\mathrm{d}\frac{\theta}{\mathrm{T}} \tag{5}$$

Where θ_{D1} and θ_{D2} are the Debye temperatures, s_1 and s_2 are the oscillator strengths, and R is the molar Boltzmann constant.[5] The model parameters from the least-squares refinement to the data for $T > 25$ K are given in Table-SVII. The total oscillator strength $s_1+s_2 = 5.18(6)$. This is in good agreement with the expected value of 1+2+2 = 5, the total number of atoms per formula unit in $EuZn_2P_2$.

For $EuMn_2P_2$, once the phonons of $EuZn_2P_2$ were calculated, the phonons were normalized to $EuMn_2P_2$ using equation:

$$\frac{\Theta^3_{L_m Y_s Z_p}}{\Theta^3_{X_m Y_n Z_q}} = \frac{mM_X^{3/2}+nM_Y^{3/2}+qM_Z^{3/2}}{mM_L^{3/2}+sM_Y^{3/2}+pM_Z^{3/2}} \tag{6}$$

where $\Theta^3_{L_m Y_s Z_p}$ and $\Theta^3_{X_m Y_n Z_q}$ are the normalization factor of $EuMn_2P_2$ and $EuZn_2P_2$, $mM_X^{3/2} + nM_Y^{3/2} + qM_Z^{3/2}$ and $mM_L^{3/2} + sM_Y^{3/2} + pM_Z^{3/2}$ are the molar masses of $EuMn_2P_2$ and $EuZn_2P_2$ (as 1Eu+2Mn+2P and 1Eu+2Zn+2P). The normalization factor outputted is 1.026 respectively.[5,6]

The electrical transport operation (ETO) option was utilized to carry out the electrical transport at low temperatures, T=2-100K. All measurements were done using the inbuilt ETO option in the PPMS. This measurement was done with angle, magnetic field, and temperature dependence on voltage and current behavior. The input current was manually changed at every temperature in consideration of the insulating nature of $EuMn_2P_2$. The applied magnetic field with 1T intervals between $\mu_o H$=0-9T and a temperature interval of T=2-20K with 1K intervals. These electronic resistivity measurements are performed using a two-probe configuration with the longitudinal and transverse resistivity probes connected to independent measurements channels. As the contacts are manually fabricated with silver epoxy, the measured data may exhibit effects of asymmetry with magnetic field due to slight misalignments of the silver contacts.

Data was analyzed with a two-channel model as described in the text. A real Schottky diode with a series resistance has a characteristic response function of:

$$I = I_s\left(e^{\left(\frac{V_{meas}-IR_s}{nV_t}\right)} - 1\right) \quad (7)$$

Where I_s is the saturation current, nV_t is the characteristic voltage, and R_s is the series resistance. This has to then be put in parallel with a normal resistor to form the two-channel model. For fitting purposes, rewriting and symmetrizing is convenient:

$$V_{meas.} = \left(\frac{I_O}{|I_1|}\right)(nV_t \ln\left(\frac{|I_1|}{I_s+1}\right) + |I_1|R_s) \quad (8)$$

$$I_2 = \frac{V_{meas.}}{R_p} \quad (9)$$

$$I_{total} = I_1 + I_2 \quad (10)$$

Where I and $V_{meas.}$ are the raw data for at a given temperature, applied field, and sample angle.

Thermal Analysis Measurements: were performed utilizing a Netzsch DSC 404 C instrument. Approximately 20 mg of the sample in a glassy carbon crucible (L2.5 mm, l=5 mm) was sealed in a Nb ampule (L=5 mm, l=15 mm). The samples were heated under an Ar atmosphere with a heating rate of 10Kmin^{-1} to T=450-580K and then cooled to 100 °C with a cooling rate of 10 Kmin^{-1}.

^{31}P NMR: ^{31}P MAS NMR spectrum was recorded on Bruker AVANCE-II spectrometer at 4.7 T magnetic field (^{31}P NMR frequency of H_3PO_4 reference 80.987 MHz) using home built MAS probe for 1.8 mm od Si_3N_4 rotors. The spectrum was obtained with spin echo pulse sequence p/2 – t – p – t - rec, where p/2 = 1.7 ms, the echo delay was one sample rotation period t = t_r = 26 ms, and a 25 ms relaxation delay between the accumulations. 32k averages have been summed for a spectrum. Since the spectrum width is a bit larger than the excitation window, we used frequency sweep with 1a 50 kHz step of excitation and summed together for the total spectrum given in Fig. 1. The sample spinning rate was 42 kHz. The chemical shift is given respective to the resonance frequency of H_3PO_4. Spin-lattice relaxation of ^{31}P was found to be exponential T_1 = 56 ms, as measured by inversion recovery pulse sequence. The ^{31}P Knight shift temperature dependence was acquired at four temperatures from 295K down to 80K. Both the susceptibility and broadening of the spectra followed the Curie-Weiss behavior. The ^{31}P Knight shift $K(T)$ follows perfectly the susceptibility curve $\chi(T)$. The χ vs K relation can be written as

$$K(T) = K_0 + \frac{H_{\rm hf}}{N_A\mu_B}\chi \quad (11)$$

where K_0 is the temperature-independent shift and $H_{\rm hf}$ is the hyperfine field. From K vs χ fit we found a hyperfine field value of $H_{\rm hf}$ = 4.0 kOe/μ_B.

^{151}Eu ZF-NMR: ^{151}Eu powder sample ZFNMR measurements of $EuMn_2P_2$ at T = 4.2 K were collected on a AVANCE II spectrometer with a home-built low temperature probe immersed in the liquid helium in dewar. The spin-5/2 nucleus shows 5 possible transitions in the spectra. When the magnetic moment of the nuclei is aligned with the quadrupolar field the gap between the peaks is uniform. Here, the middle transition has a different location, which refers to an angle between the two fields. In $EuMn_2P_2$ the electric field gradient (EFG) tensor is symmetric and perpendicular to the *c*-axis. Exact resonance frequencies can be calculated by the nuclear spin Hamiltonian

$$\mathcal{H} = -\gamma_n\hbar\boldsymbol{I}\cdot\boldsymbol{H}_{\rm int} + \frac{h\nu_Q}{6}\left[3I_z^2 - I(I+1) + \frac{1}{2}\eta(I_+^2 + I_-^2)\right] \quad (12)$$

where the first term represents the Zeeman interaction between the nuclear magnetic moment $\boldsymbol{\mu}_{\rm n} = \gamma_n\hbar\boldsymbol{I}$ and the internal magnetic field $\boldsymbol{H}_{\rm int}$. The second term represents the nuclear quadrupolar interaction between the EFG and the nuclear quadrupolar moment, where $\nu_Q = \frac{3e^2Qq}{2I(2I-1)h}$ is the nuclear quadrupolar frequency and η is a symmetry parameter of the EFG tensor. Here eQ is the electric quadrupole moment of

the nucleus and $eq = V_{zz}$ is the main principal value of the EFG tensor, $\eta = \frac{V_{xx}-V_{yy}}{V_{zz}}$. The operators are transformed from the crystal frame to the Laboratory frame using Euler angles in the ZYZ convention, after which the eigenvalues of eq. (12) are found. The differences of the eigenstates represent the transition energies, five of which have a probability to occur. The calculated results offer a good match with the experiment and we acquired values for the quadrupolar frequency, strength of the internal field and the angle of the quadrupolar field. The parameter errors were estimated with standard deviation in the error regions of the experimental data fittings.

^{151}Eu Mössbauer spectroscopy: The ^{151}Eu ME measurements at ambient pressure in the temperature range 300–1.75 K were carried out on these samples using a 100 mCi $^{151}SmF_3$ source. Both source and absorber were kept at the same temperature in a top-loading cryostat. Mössbauer spectra were analyzed with the NORMOS software package,[7] to derive pertinent hyperfine interaction parameters, isomer shift S, magnetic hyperfine field B_{eff}, and absorption areas (abundances) of spectral components. All isomer shift values are quoted relative to the SmF_3 source from here onwards.

Finite element analysis: Thermomagnetoelectric finite element simulations were carried out using Ansys Discovery AIM version 2019 R3. Geometric parameters were taken from those used in experiment. The base temperature was fixed at T = 2 K, with electrical and thermal conductivities of the PCB board, grease, and silver epoxy taken from literature values. The temperature-dependent electrical conductivity of $EuMn_2P_2$ were extracted from the I→0 limit of the IV curves. Based on literature values for isostructural compounds, the thermal conductivity of $EuMn_2P_2$ was set to be 1 W/m/K. Radiative losses at the surfaces was included, assuming a surrounding vacuum. Different variations of these simulations (slight changes in parameters, inclusion or not of radiative effects, etc), not shown, did not change the qualitative result of increased joule heating by 1μA of current.

Fig. S1 Differential scanning calorimetry measurements of $EuMn_2P_2$ single crystals for T=450-580K. At T=510K there is a phase transition attributed to the melting of incompletely removed Sn flux.

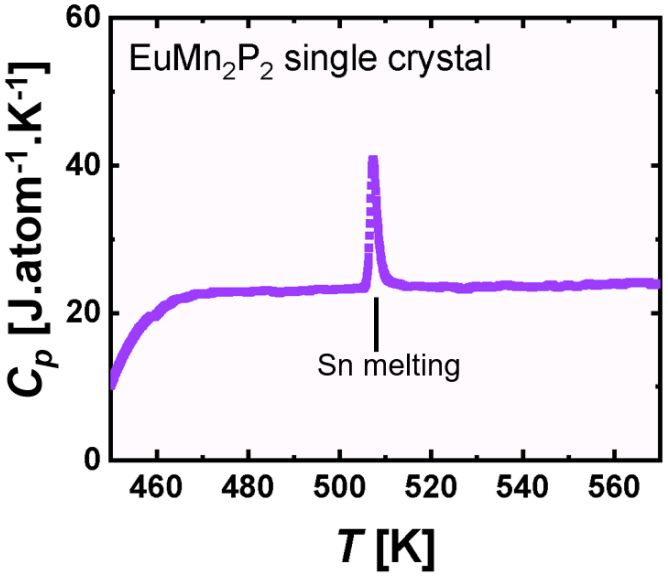

Fig. S2 High temperature magnetization of $EuMn_2P_2$ single crystals shows no evident magnetic phase transitions corresponding to Mn^{2+}.

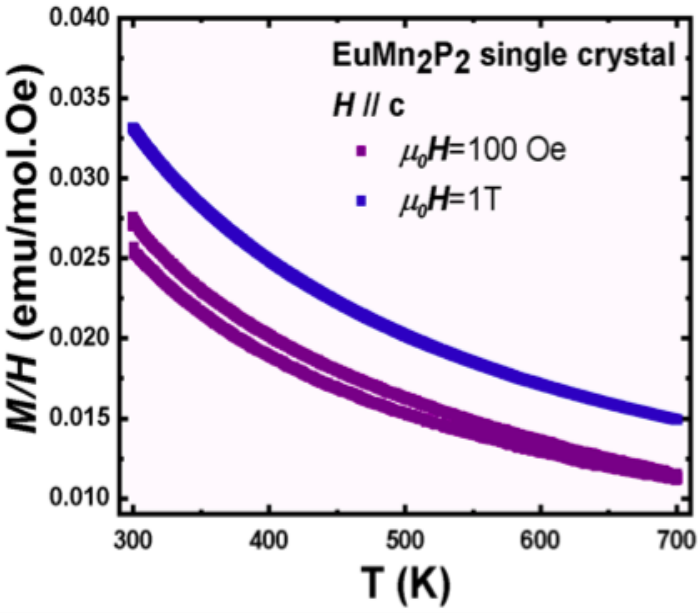

Fig. S3 (a) Four probe resistivity of $EuMn_2P_2$ single crystals at T=200-400K. **(b)** Natural logarithm of normalized resistivity as a function of $\frac{1}{T}$ measured on a single crystal of $EuMn_2P_2$ along the c-axis. The bandgap extrapolated is E_g=0.2eV and is fit to $\ln\left(\frac{\rho}{\rho_{T=400K}}\right) = \frac{E_g}{k_B}\frac{1}{T}$.

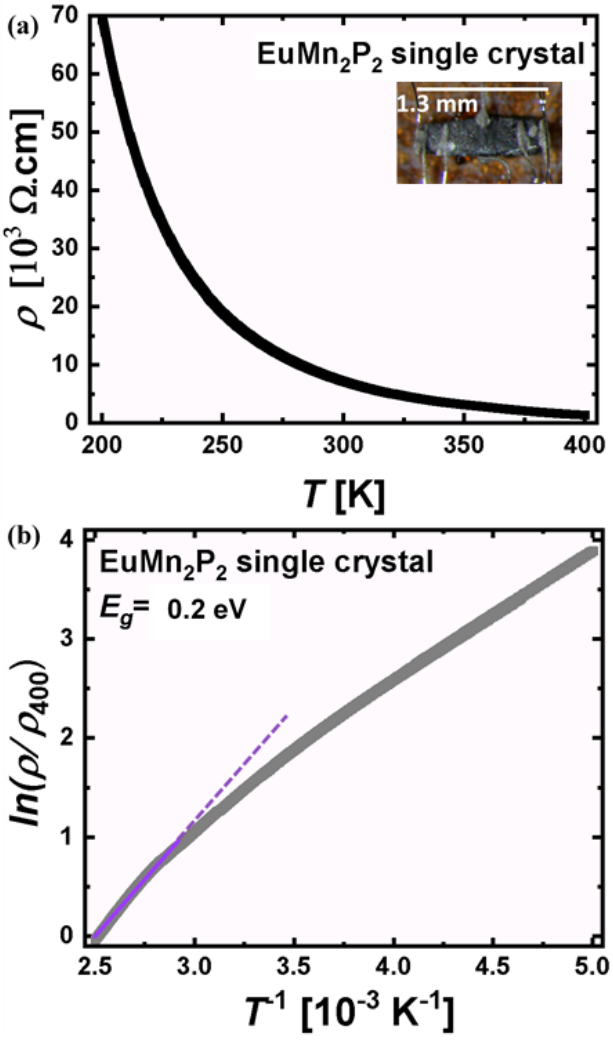

Fig. S4 Optical spectroscopy to determine the (a) transmission and (b) conductivity of $EuMn_2P_2$ single crystals. These data are consistent with a sharp band edge at 0.68eV, with a tail of states extending down from the band edge to ~2000 cm^{-1} (~0.2 eV), in agreement with transport measurements. The sharp absorption features in the 500-1800 cm^{-1} range are IR active phonon modes.

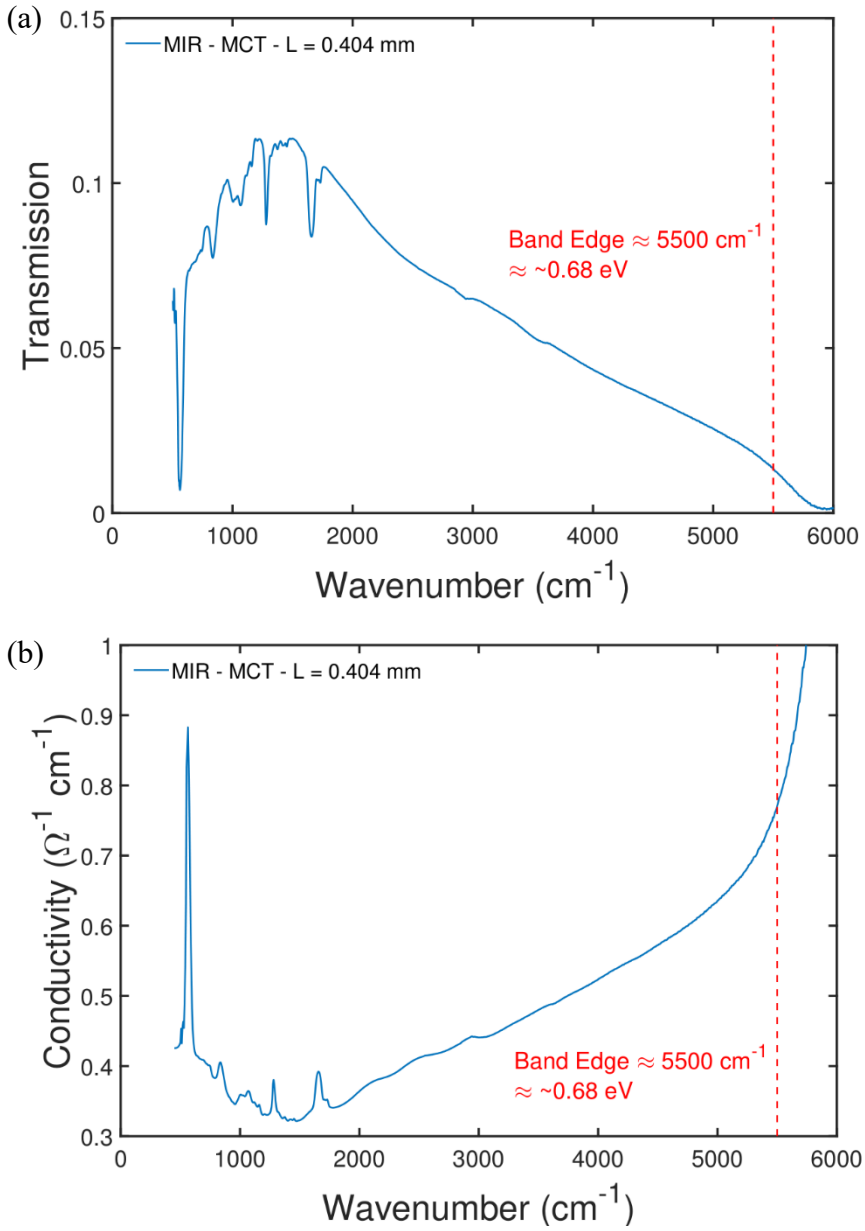

Fig. S5 Temperature dependence of magnetic susceptibility of $EuMn_2P_2$ single crystal **(a)** and powder sample **(b)** The cyan-colored lines represent Curie-Weiss fitting, measured under the magnetic field used in ^{31}P NMR experiments. The blue dots in graph (b) show the Knight shift temperature dependence. The inset shows a linear relation of χ vs K which corresponds to a Hyperfine field value of $H_{hf} = 4.0$ kOe/μ_B.

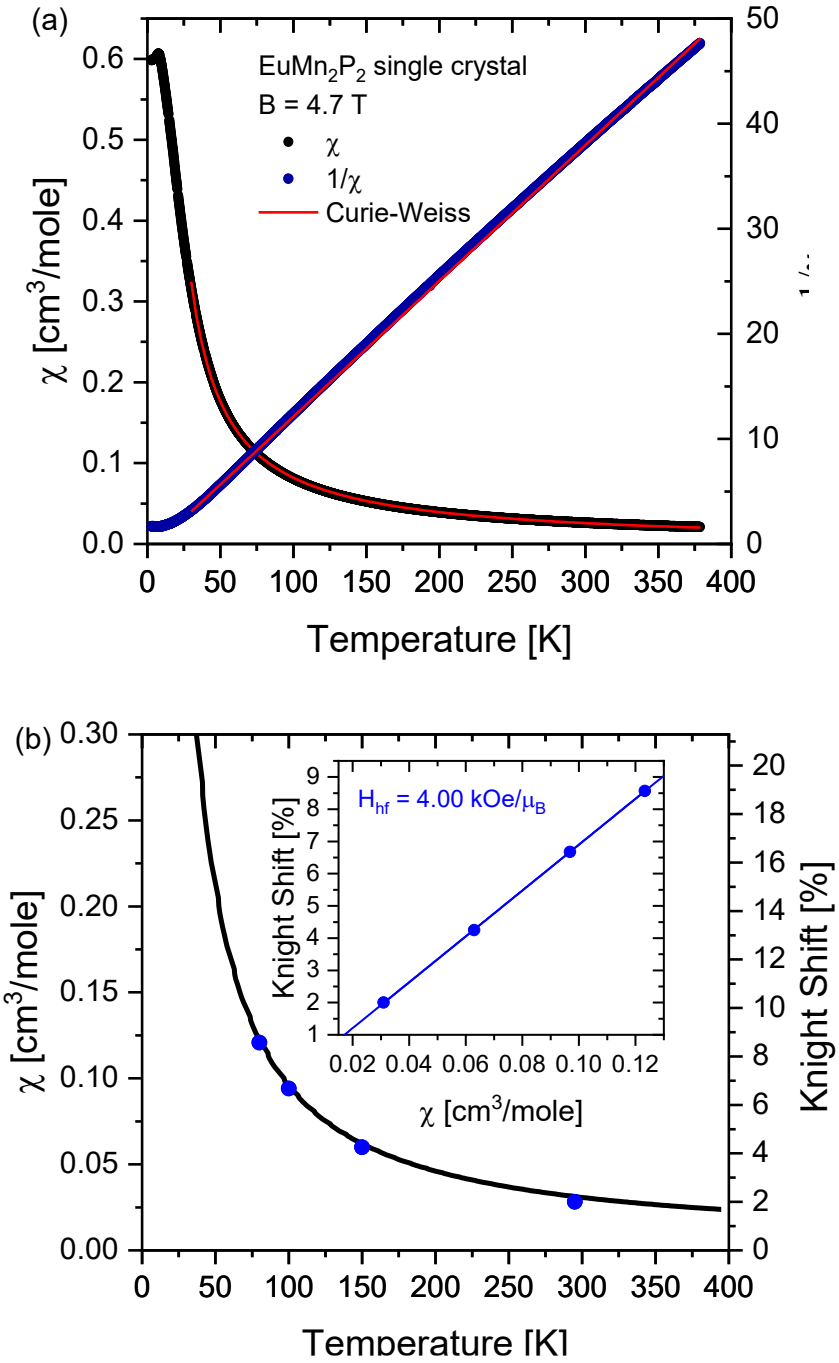

Fig. S6 ^{31}P NMR spin-lattice relaxation (Blue) and spin-spin relaxation (red) time temperature (in) dependence of $EuMn_2P_2$. In range of the error bars both relaxations show almost constant behavior.

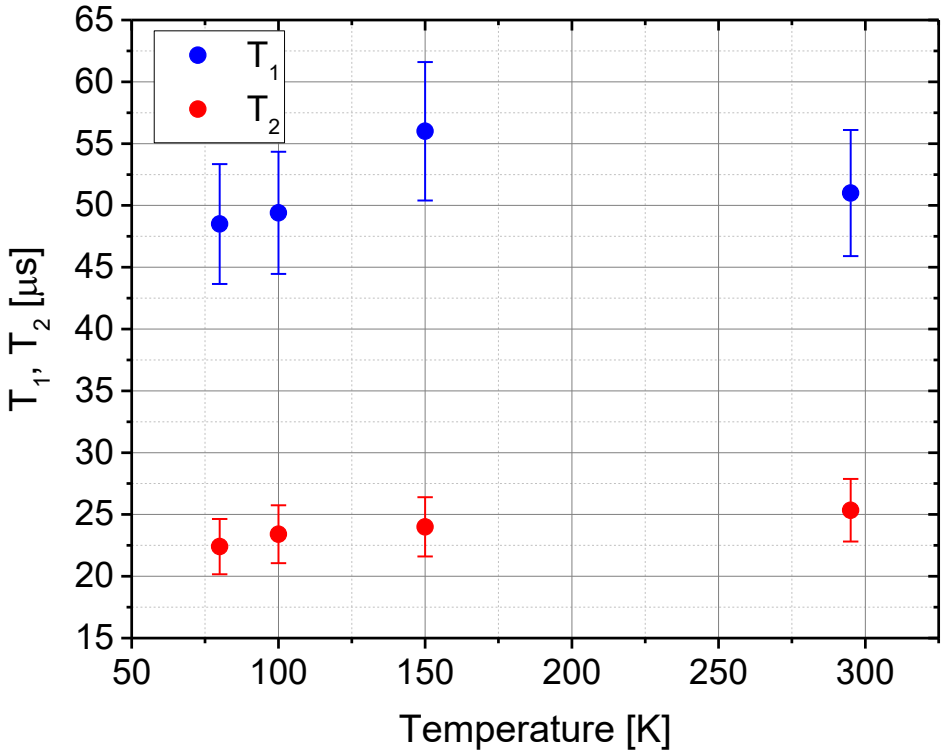

Table SI. Two-Debye model parameters used to describe the $EuMn_2P_2$ phonons. The oscillator strengths were fixed to those found for $EuZn_2P_2$, and the Debye temperatures adjusted to account for the molecular mass difference between Mn and Zn.

Single crystals	**s_{D1} (oscillator strength/formula unit)**	**s_{D2} (oscillator strength/formula unit)**	**θ_{D1}(K)**	**θ_{D2}(K)**
$EuMn_2P_2$	2.8	2.83	506(2)	182.3(6)

Fig. S7 Temperature dependence of the fitted hyperfine field contributions in $EuMn_2P_2$ derived from the modulated model. **(a)** The average hyperfine field (B_{avg}) is plotted as solid round symbols with a dotted line showing a fit yielding a transition temperature of 18 K. **(b)** fluctuation rate derived from dynamic fits derived from the dynamic distribution fits.

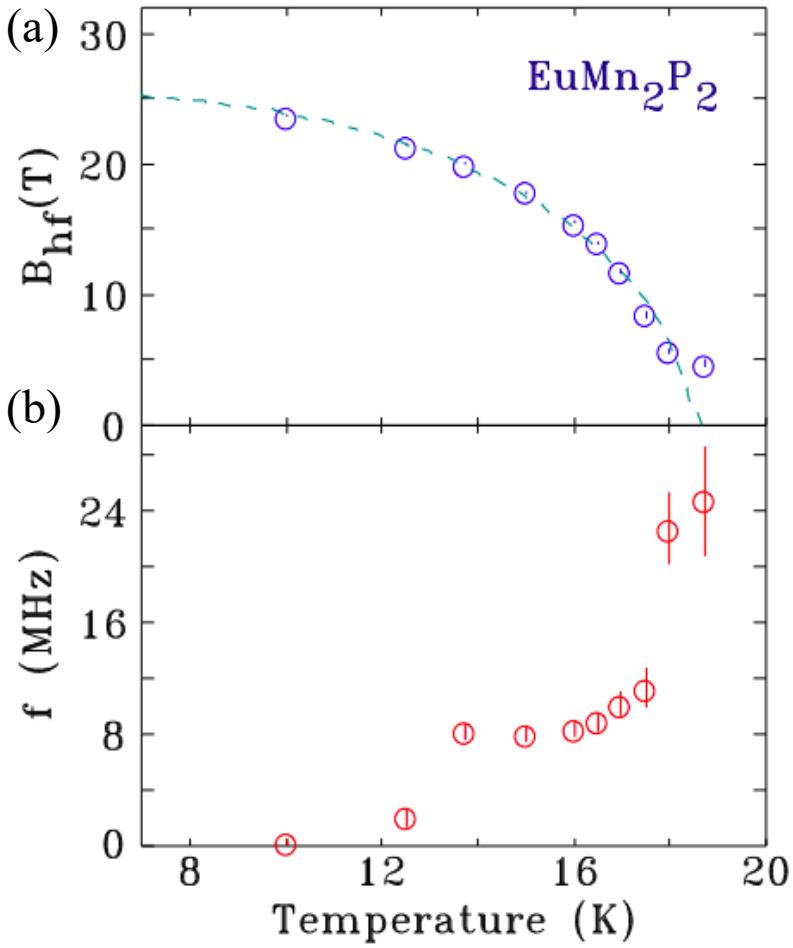

Fig. S8 ^{151}Eu NMR measurement in zero applied field represented with black squares. The blue line represents a fitting done with the five transition frequencies acquired from the Hamiltonian with the provided parameters.

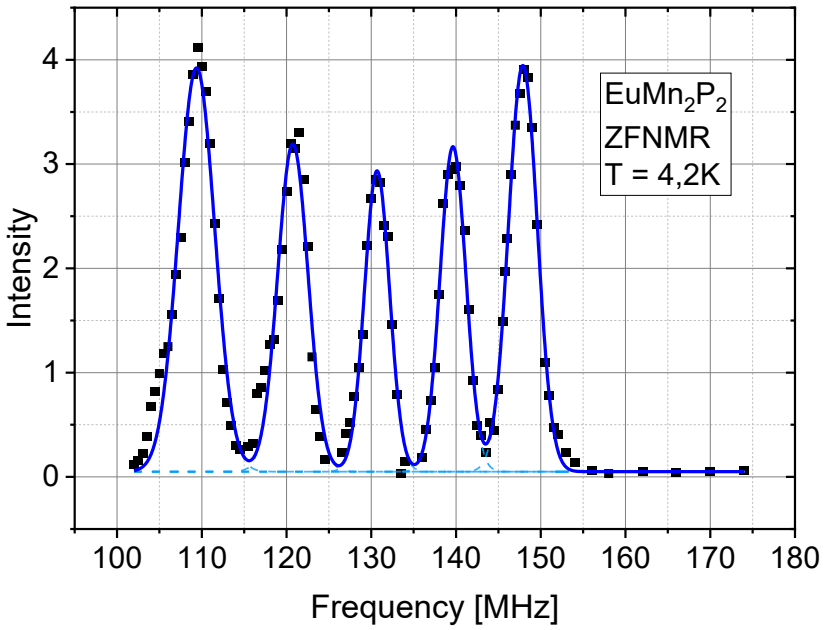

Table SII. Experimental and calculated transition frequencies in the spectrum of ^{151}Eu ZFNMR of $EuMn_2P_2$, at T = 4.2K The calculation parameters: $\nu_Q = 19.47 \pm 0.03$ MHz, asymmetry of the EFG tensor: $\eta = 0$, Larmor frequency $\nu_L = 129.28 \pm 0.13$ MHz, corresponds to the internal field at Eu nucleus $\boldsymbol{H}_{\text{int}} = \mathbf{12.32}$ T, and angle between the magnetic moment and quadrupolar tensor $\theta =$ $87.12 \pm 1{,}07$ degrees.

Transition m =	Exp (MHz)	Standard dev (MHz)	Calc (MHz)
-5/2 ↔-3/2	147.884	0.0576	147.890
-3/2 ↔ -1/2	139.663	0.0664	139.642
-1/2 ↔ +1/2	130.656	0.0707	130.681
+1/2 ↔+3/2	120.758	0.0714	120.746
+3/2 ↔+5/2	109.374	0.0634	109.376

Table SIII Single crystal x-ray diffraction (SXRD) parameters and refinement statistics.

Formula	**$EuMn_2P_2$**
Crystal system	Trigonal
Space Group	*P-3m1* (No. 164)
a (Å)	4.136
b (Å)	4.136
c (Å)	7.005
V ($Å^3$)	103.776704
Z	1
M/$gmol^{-1}$	323.78
ρ_0/gcm^{-3}	5.181
μ/mm^{-1}	21.452
Radiation	Mo Kα, λ = 0.71073 Å
Temperature (K)	293 K
Reflections collected	2632
Unique Reflections	186
Refined Parameters	9
Goodness-of-fit	1.323
R[F][a]	0.0076
$R_w(F_o^2)$[b]	0.021

[a] $\mathbf{R(F) = \Sigma||F_o| - |F_c||/\Sigma|F_o|}$

[b] $\mathbf{R_w(F_o^2) = [\Sigma w(F_o^2 - F_c^2)^2/\Sigma w(F_o^2)^2]^{1/2}}$

Table SIV Atomic coordinates for $EuMn_2P_2$ determined by SXRD

	Occ.	**Wyckoff Positions**	**x (Å)**	**y (Å)**	**z (Å)**	**U_{eq} ($Å^2$)**
Eu	1	1a	0	0	0	0.00329(6)
Mn	1	2d	2/3	1/3	0.62080(6)	0.00401(9)
P	1	2d	2/3	1/3	0.26921(10)	0.00412(13)

Table SV Anisotropic displacement parameters for $EuMn_2P_2$ determined by SXRD

	U(1,1)	**U(2,2)**	**U(3,3)**	**U(1,2)**	**U(1,3)**	**U(2,3)**
Eu	0.00323(7)	0.00323(7)	0.00340(9)	0.00161(4)	0	0
Mn	0.00412(12)	0.00412(12)	0.0380(17)	0.00206(6)	0	0
P	0.0041(2)	0.0041(2)	0.0042(3)	0.00203(10)	0	0

Fig. S9 (a) Band structure and density of states of $EuMn_2P_2$ within GGA+U considering an A-type antiferromagnetic order with U = 5eV on the Eu atoms and non-magnetic Mn atoms. A metallic behavior is predicted in agreement with the expectation that a non-spin polarized d-shell should not have an energy gap. (b) Band structure and density of states for $EuMn_2P_2$ within GGA+U with A-type antiferromagnetic order and U = 5eV for Eu and C-type antiferromagnetic and U = 5eV for Mn. These contributions result in a prediction of semiconducting behavior for $EuMn_2P_2$. The physical mechanism is the antiferromagnetic order in Eu suppresses spin up to spin down hoppings t, where $t < U$ and thus resulting in a Mott insulator. Further, within the crystal structure of $EuMn_2P_2$ we notice that the Mn and P units are bonded covalently in tetrahedra, whereas Eu layers behave as Van der Waals layers with weak J coupling with one another. These bonding interactions signify that the close bonding in the Mn-P units corresponds to the density of states close to the Fermi level and the weak Eu bonding is further away from the Fermi level.

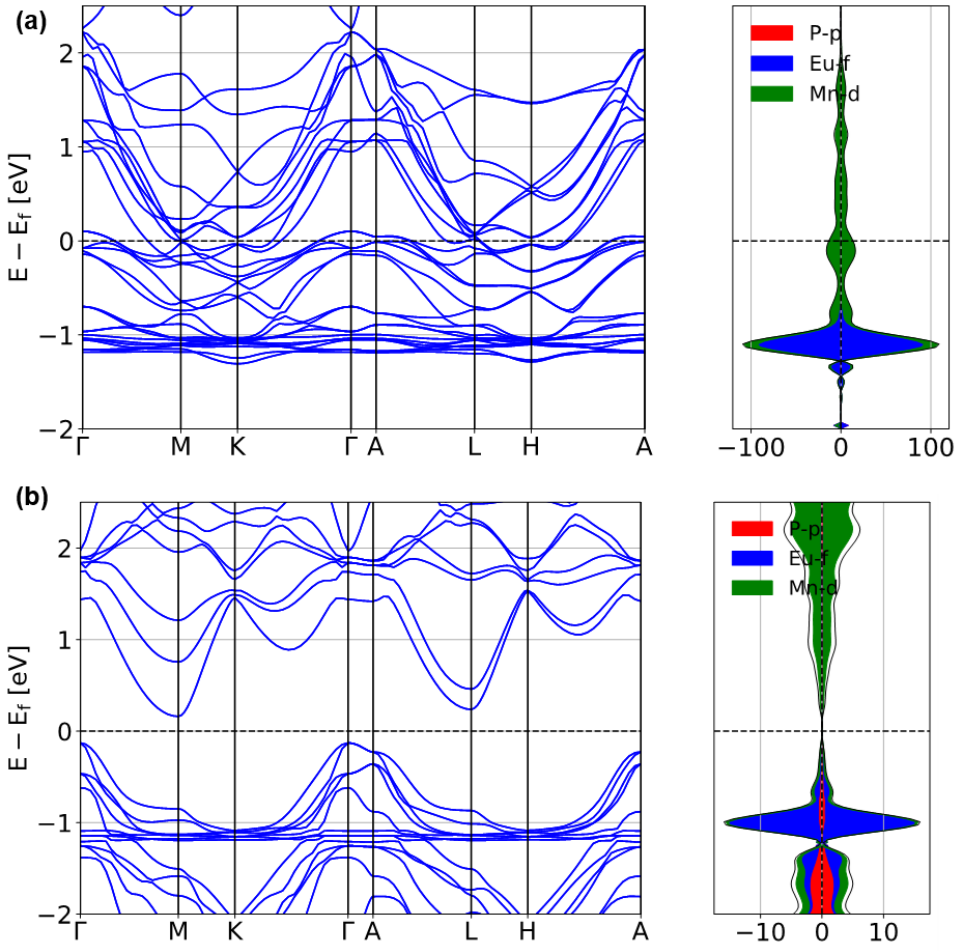

Fig. S10 Band structure and density of states of $EuMn_2P_2$ within GGA+U. For the Eu atoms we consider an A-type antiferromagnetic order, with U=5eV. For Mn we consider **(a)** a C-type antiferromagnetic order with U=0eV, or **(b)** ferromagnetic order with U=5eV. In both cases DFT predicts metallicity for $EuMn_2P_2$ and illustrates that antiferromagnetic order or Hubbard U alone are not suffiecient to explain the observed semiconducting behavior.

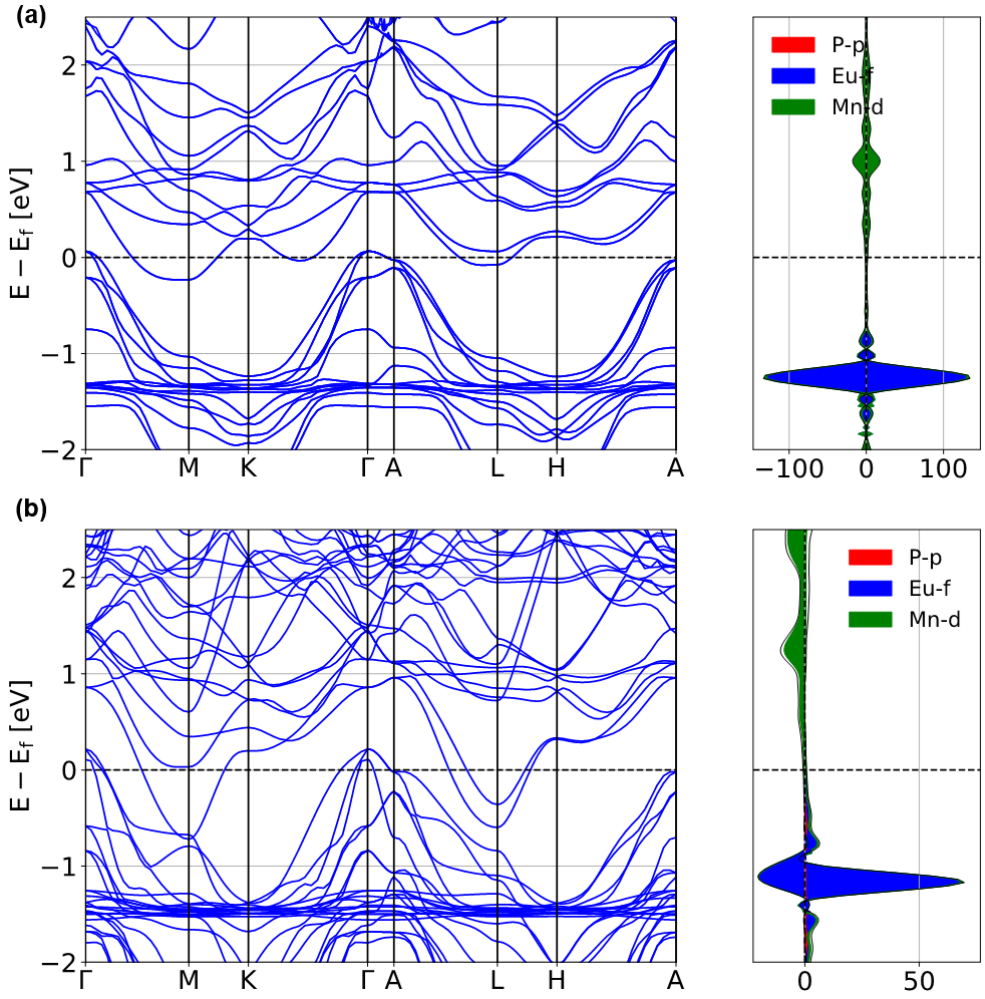

Fig. S11 Band structure for the predicted magnetic configuration (a) without (b) with spin orbit coupling (SOC) shows Evidence that the effect of SOC is negligible. Also, the parity criterion confirms that it is topologically trivial. In addition, we used the Fu-Kane parity criterion to confirm that the $EuMn_2P_2$ is a topologically trivial insulator.

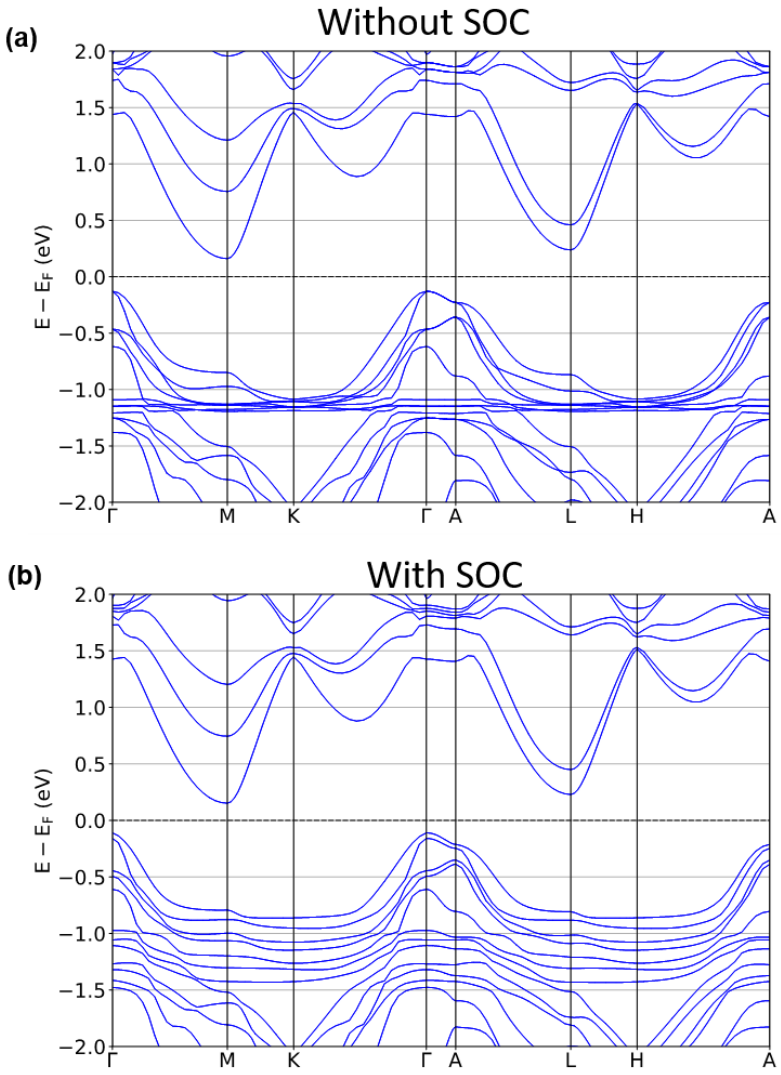

Fig. S12 Comparison between different putative antiferromagnetic orders for the Mn atoms. **(a)** Within GGA+U, the C-type antiferromagnetic order is predicted to be the lowest in energy compared to other putative antiferromagnetic orders. **(b)** This agrees with the observation of a sharp phase transition when Eu atoms magnetically order at 17K due to lowering of the symmetry. **(b)** For a G-type antiferromagnetic order, a sharp phase transition is not expected when Eu atoms magnetically order.

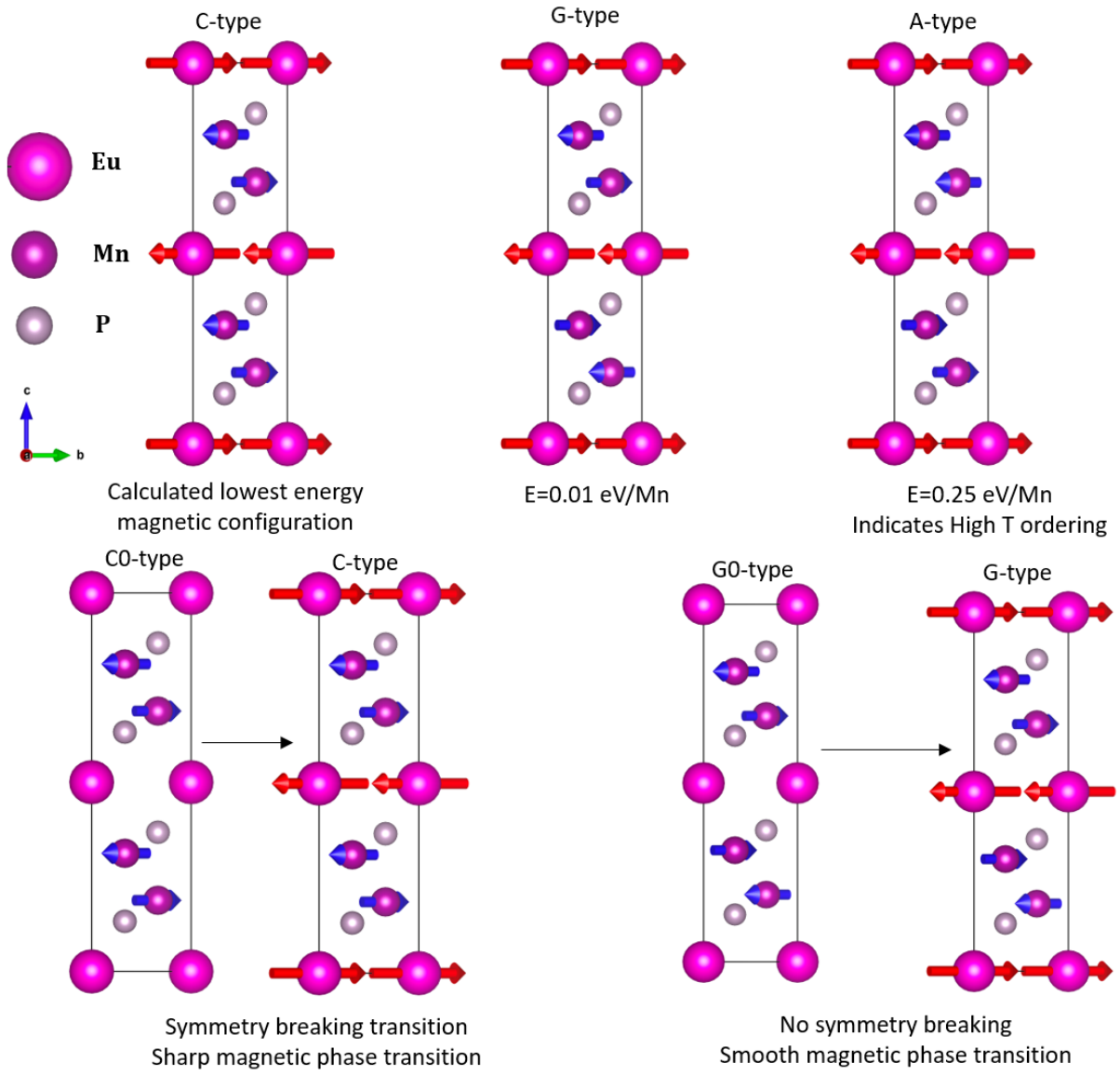

Fig. S13 The mechanism of the switch on of non-linear voltage-current behavior in the single crystals of $EuMn_2P_2$ with the onset of Eu magnetic order at T_N=17K. **(a)** Above T_N, the IV curve is linear, and the indirect gap is 0.445 eV. Conduction is thus dominated by an impurity band located somewhere in the gap, shaded orange. **(b)** When the Eu atoms magnetically order, there is a large exchange splitting of the $(Mn_2P_2)^{2-}$ derived conduction band states. This reduces the indirect gap to 0.29 eV, and makes accessible a second set of states (from the conduction band), when an appropriate voltage is applied to the metallic contacts. This gives rises to impurity-band-driven transport at low voltages, and impurity-and-conduction band driven transport at high voltages.

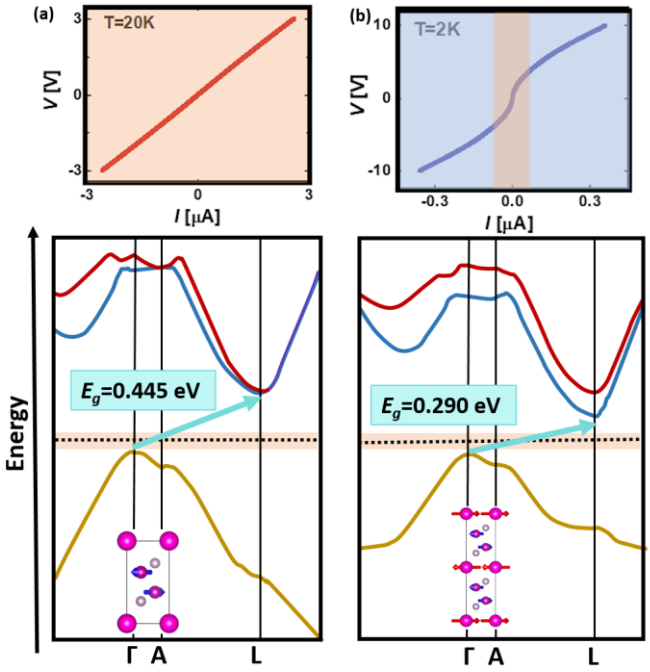

Fig. S14. The onset of nonlinear voltage current behavior below the Eu magnetic ordering temperature of T_N=17K in $EuMn_2P_2$ single crystals as seen in **(a)** T=20K, **(b)** T=15, **(c)** T=5K, and **(d)** T=2K. **(e)** The magnetic field dependence of voltage current behavior with $\mu_oH\perp$c at T=2K showing the non-linear behavior is only slightly affected by an applied magnetic field. **(f)** The correlation between the hyperfine field from Mössbauer spectroscopy with the fraction diode current model at μ_oH=0T and μ_oH=9T, showing the "turn on" of non-linear behavior with the appearance of antiferromagnetic order on Eu. **(g)** The resistance, dV/dI, as a function of potential difference at μ_oH=0T and μ_oH//c. The blue frame is the region where $V\rightarrow0$ pertaining to the conduction channel associated to the non-linearity in the voltage-current plots. **(h)** The temperature dependence of the resistance associated as $V\rightarrow0$ from the blue region in (g) at μ_oH=0T and μ_oH//c. **(i)** The normalized resistivity in (h), but plotted vs. $\frac{1}{T^{1/2}}$. A $T^{1/2}$ scaling is suggestive of 1-dimensional variable-range-hopping in the $V\rightarrow0$ from the blue region in (g) at μ_oH=0T and μ_oH//c.

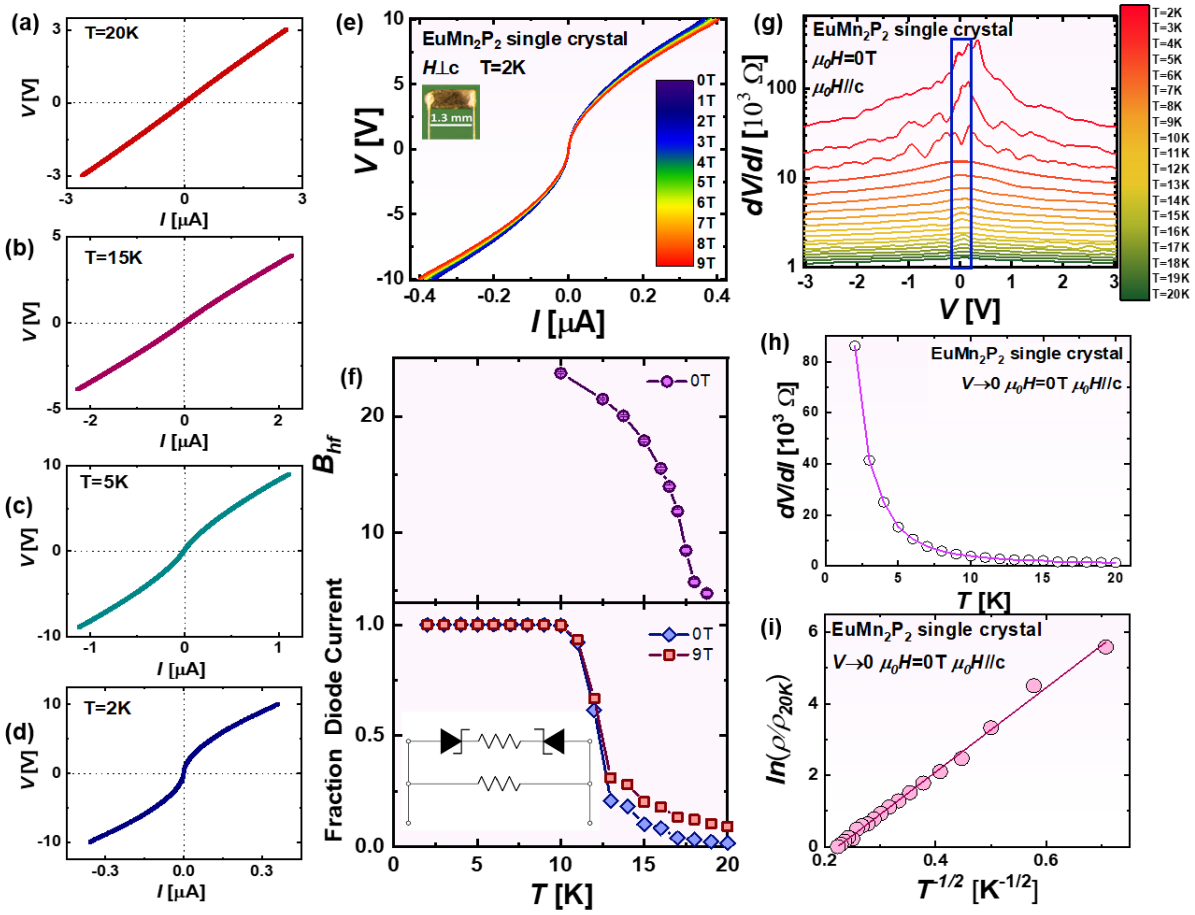

Fig. S15 Alternative view of the I-V behavior: differential resistance, *dV/dI,* for $\mu_o H$||c as a function of voltage at **(a) T**=2K, **(b)** T=5K, and **(c)** T=10K.

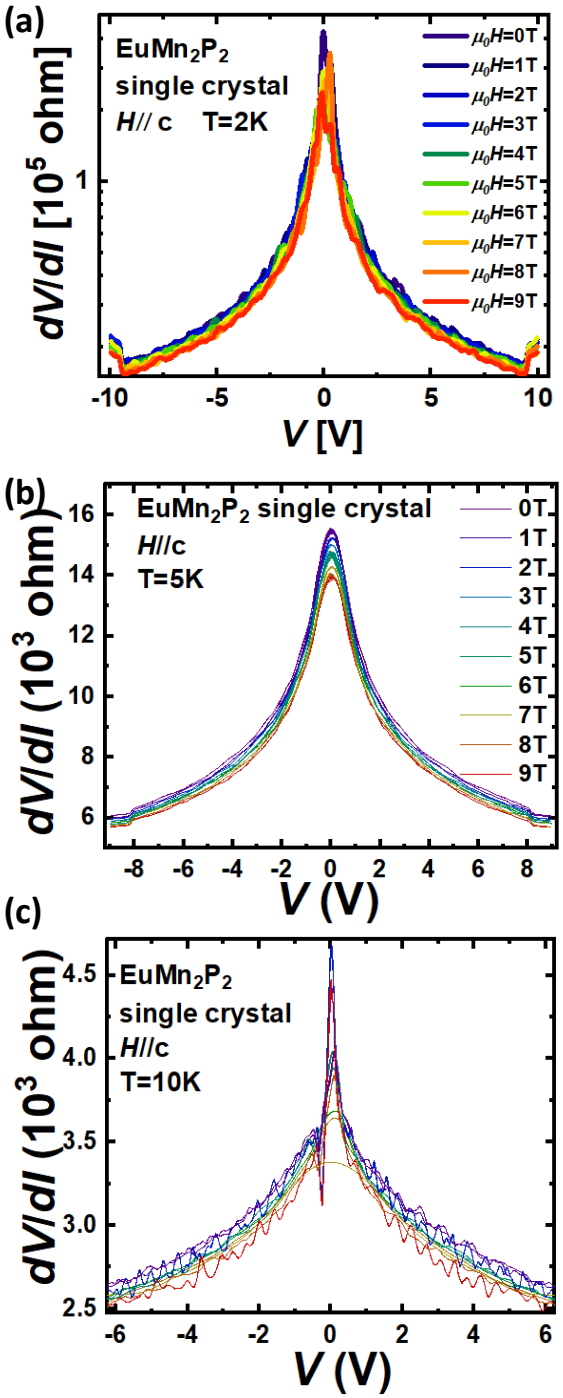

Fig. S16 (a) Resistance, *dV/dI* at $\mu_o H$ ||c as a function of voltage T=2K at $\mu_o H$=0T. The differential resistance is broken up in channels, reflecting the low and high voltage responses respectively. Channel-1 is denoted at the low voltage and channel-2 is denoted as the high voltage response. **(b)** The temperature dependence of channel-1. **(c)** The temperature dependence of channel-2. As expected for an insulator, the decrease in resistance as the temperature is increased in (b) and (c). **(d)** The same normalized resistivity in (b), but plotted vs. $\frac{1}{T^{1/2}}$. A $T^{1/2}$ scaling is suggestive of 1-dimensional variable-range-hopping (VRH) in the low voltage region. **(e)** The same normalized resistivity in (c), but plotted vs. $\frac{1}{T^{1/4}}$. A $T^{1/4}$ scaling is suggestive of 3-dimensional variable-range-hopping (VRH) in the high voltage region.

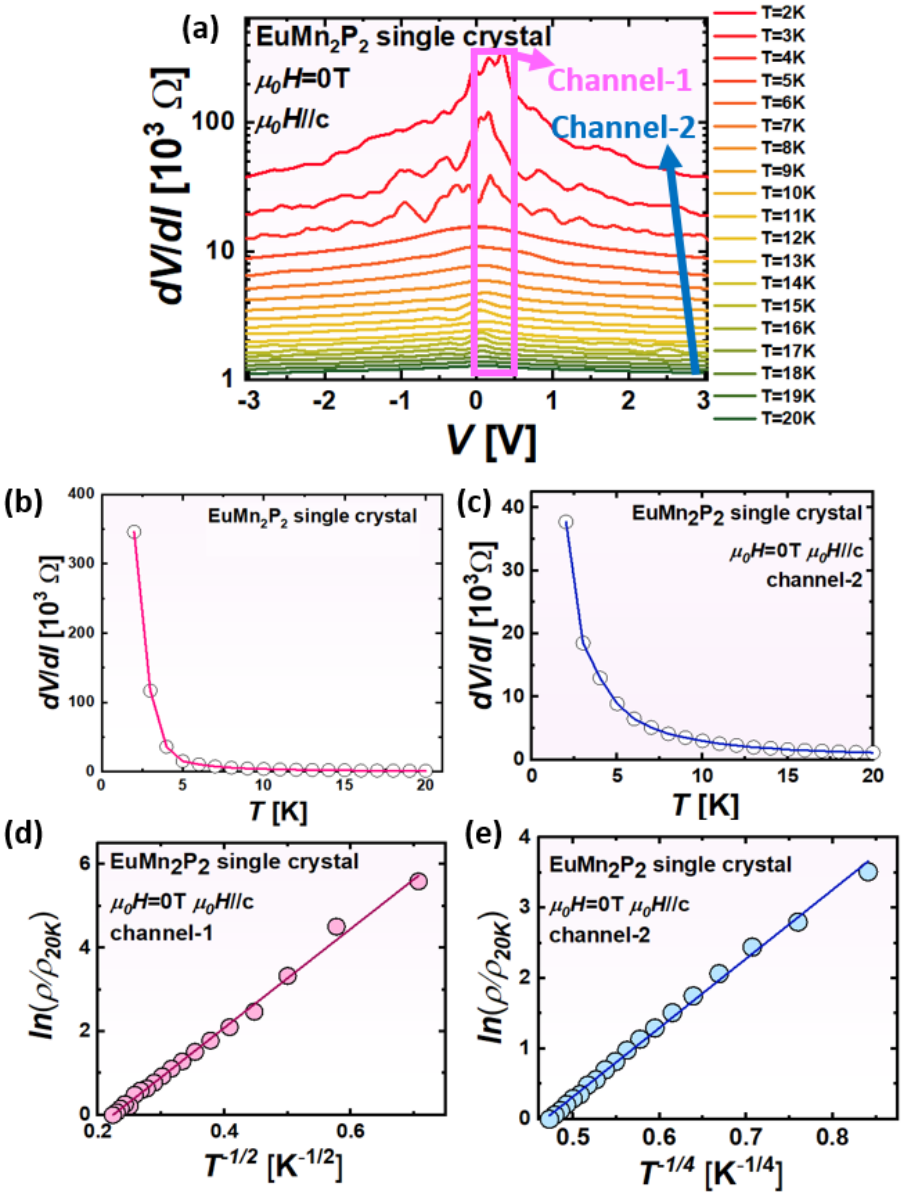

Table SVI. Quantification of the non-linear behavior in a two-channel model with i⊥c at $\mu_o H$=0T as described by the combination of equation (8), (9), and (10) in the SI.

T (K)	nV_t (V)	R_s (Ω)	I_s (A)	R_p (Ω)
2	1.46263	13453.01	1.10×10^{-5}	4.93×10^{20}
3	0.98622	11132.51	1.78×10^{-5}	4.79×10^{19}
4	0.90182	8309.404	3.92×10^{-5}	4.84×10^{10}
5	1.50788	5090.016	1.38×10^{-4}	2.70×10^{10}
6	1.52124	4050.199	2.29×10^{-4}	2.70×10^{9}
7	1.24701	3899.045	2.22×10^{-4}	41228.02
8	0.99289	3352.601	2.99×10^{-4}	54326.12
9	1.68091	2459.097	6.80×10^{-4}	63239.63
10	1.28865	2261.202	7.66×10^{-4}	118603.8
11	0.92313	2544.819	4.48×10^{-4}	11069.33
12	1.28358	2597.081	4.79×10^{-4}	5849.598
13	0.61154	3434.207	1.47×10^{-4}	3637.912
14	0.69954	4146.982	1.03×10^{-4}	2742.348
15	0.65008	3543.032	1.14×10^{-4}	2536.328
16	0.50423	6332.828	1.79×10^{-5}	1876.715
17	0.47924	6386.381	1.88×10^{-5}	1713.698
18	0.36378	7733.925	7.27×10^{-6}	1534.904
19	0.36783	7573.468	7.24×10^{-6}	1416.138
20	0.36179	7234.724	8.36×10^{-6}	1320.561

Fig. S17 (a) Resistance, *dV/dI* at $\mu_o H$ ||c as a function of voltage T=2K at $\mu_o H$=9T. The differential resistance is broken up in channels, reflecting the low and high voltage responses respectively. Channel-1 is denoted at the low voltage and channel-2 is denoted as the high voltage response. **(b)** The temperature dependence of channel-1. **(c)** The temperature dependence of channel-2. As expected for an insulator, the decrease in resistance as the temperature is increased in (b) and (c). **(d)** The same normalized resistivity in (b), but plotted vs. $\frac{1}{T^{1/2}}$. A $T^{1/2}$ scaling is suggestive of 1-dimensional variable-range-hopping (VRH) in the low voltage region. **(e)** The same normalized resistivity in (c), but plotted vs. $\frac{1}{T^{1/4}}$. A $T^{1/4}$ scaling is suggestive of 3-dimensional variable-range-hopping (VRH) in the high voltage region.

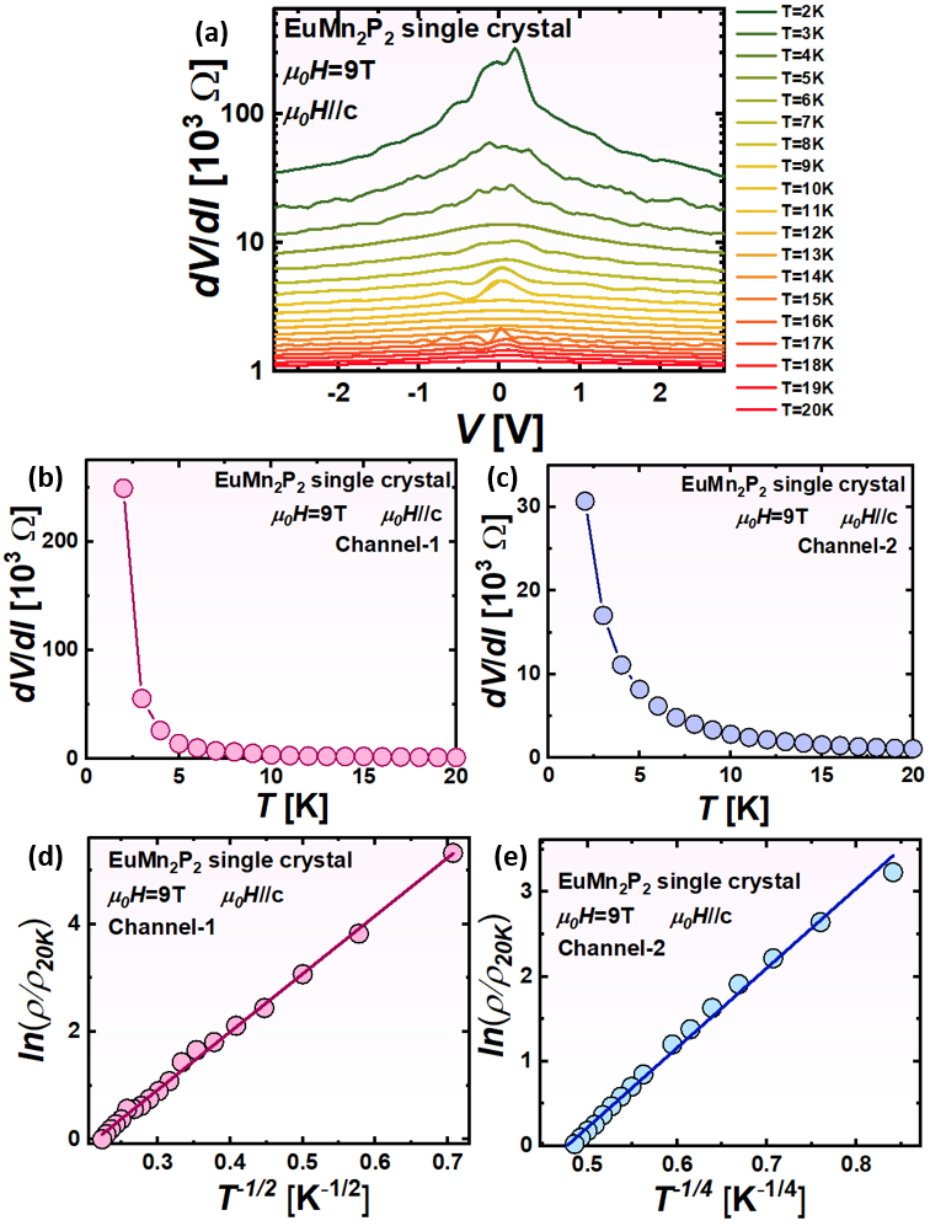

Table SVII. The table below is a derived from the combination of equation (7), (8), and (9) in the supplementary text at $\mu_o H \perp c$ and $\mu_o H$=9T.

T (K)	nV_t (V)	R_s (Ω)	I_s (A)	R_p (Ω)
2	1.38938	12481.17	1.21×10^{-5}	8.85×10^{17}
3	0.99292	10143.23	2.10×10^{-5}	1.22×10^{14}
4	0.98668	7782.008	3.63×10^{-5}	105087.0
5	0.99215	8418.093	9.84×10^{-6}	14616.88
6	0.97453	7089.717	2.34×10^{-5}	11659.76
7	1.29734	4621.303	1.28×10^{-4}	13314.81
8	0.79225	6511.687	3.10×10^{-5}	6492.985
9	1.18612	3633.853	1.81×10^{-4}	7871.676
10	1.02598	3327.602	2.43×10^{-4}	6970.228
11	1.17927	2943.889	3.48×10^{-4}	6000.555
12	1.01141	2664.900	3.96×10^{-4}	5491.424
13	0.97802	2442.924	4.88×10^{-4}	5016.348
14	0.95192	2222.205	5.79×10^{-4}	4530.668
15	0.97223	2244.757	5.46×10^{-4}	3511.671
16	0.96730	2408.785	4.56×10^{-4}	2734.356
17	0.89172	3007.707	2.23×10^{-4}	2019.601
18	0.95455	1695.951	8.97×10^{-4}	3016.451
19	0.90409	2363.399	4.30×10^{-4}	1914.135
20	0.84149	2516.778	1.11×10^{-5}	1240.173

Fig. S18 Ansys finite element simulations of current dependent heating effects for (a) 0.1 μA current, and (b) 1 μA current.

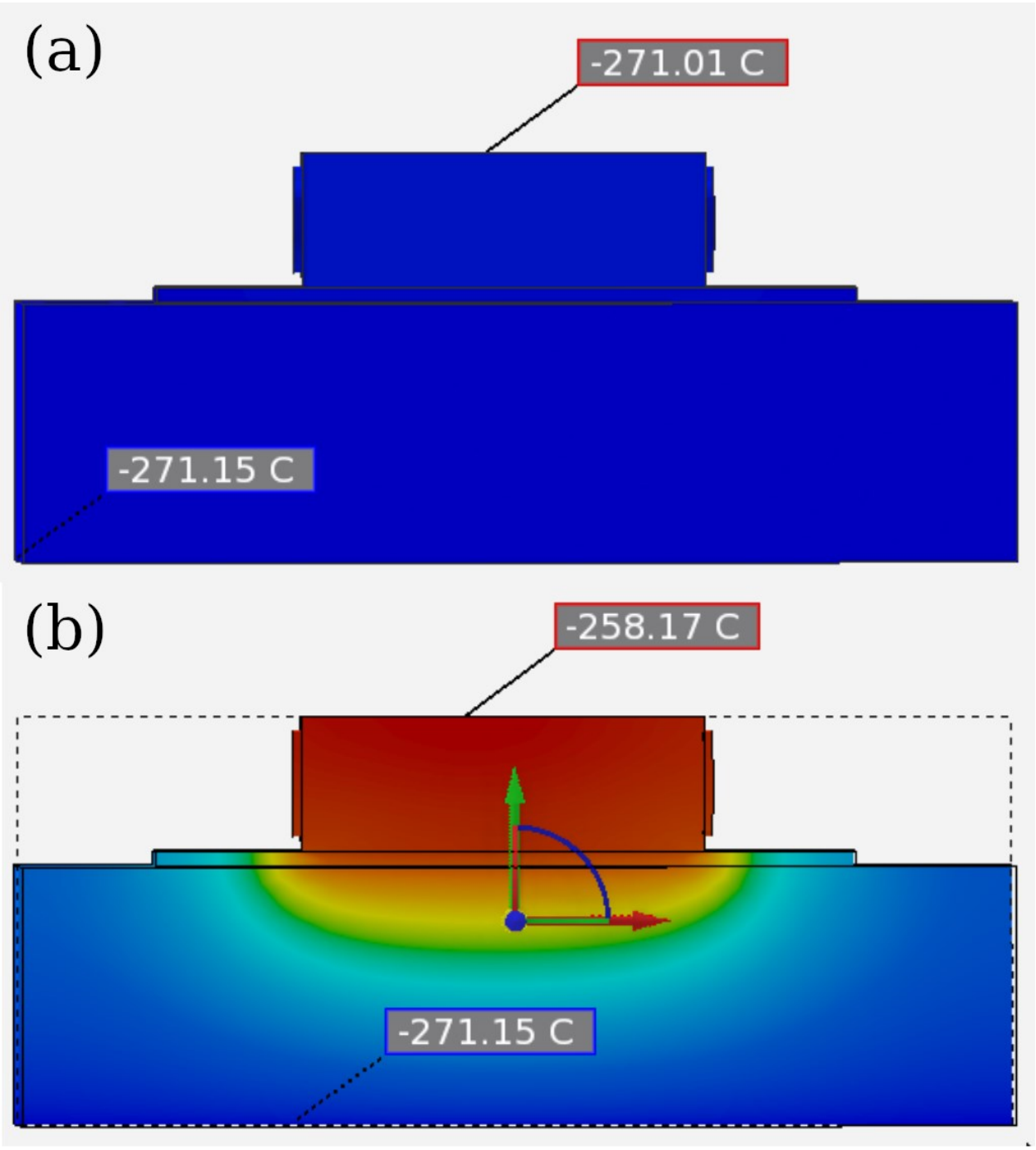

Table SVIII. The table below lists average Mn-P bond distances (Å) in known materials and a comparison to the magnetic and conducting properties.

Avg. Mn-P bond (Å)	Material	Magnetism	Conductivity	Reference
2.27873	γ MnP_4	AFM	semiconducting	8
2.35900	$LaMnCuP_2$	weak magnetic AFM	metallic	9
2.50380	CoMnP	FM	metallic	10
2.35767	MnP	FM	metallic	11
2.51350	$SrMn_2P_2$	magnetically-frustrated AFM	semiconducting	12
2.49050	$CaMn_2P_2$	magnetically-frustrated AFM	semiconducting	12
2.49375	$EuMn_2P_2$	AFM	insulating	1, This work
2.93400	$Mn_3Ni_{20}P_6$	FM	metallic	13
2.38700	$CsMn_2P_2$	AFM	metallic	14
2.27317	MnP_4	diamagnetic	semiconducting	15
2.46400	$MnSiP_2$	AFM	semiconducting	16
2.42425	ZrMnP	FM	metallic	17
2.39775	$Hf_{1.04}Mn_{1.06}P_{0.90}$	FM	metallic	17
2.58500	$Eu_{14}MnP_{11}$	FM	semiconducting	18
2.37256	Mn_3P	hellical magnetism	metallic	19
2.42678	Mn_2P	AFM	metallic	20
2.43800	$BaMn_2P_2$	AFM	semiconducting	21

Fig. S15 (a) Schematic of switch on and off in regards to magnetic ordering driven non-linear current voltage response, **(b)** Key data that supports the non-linear current voltage response at temperatures below T_N=17K.

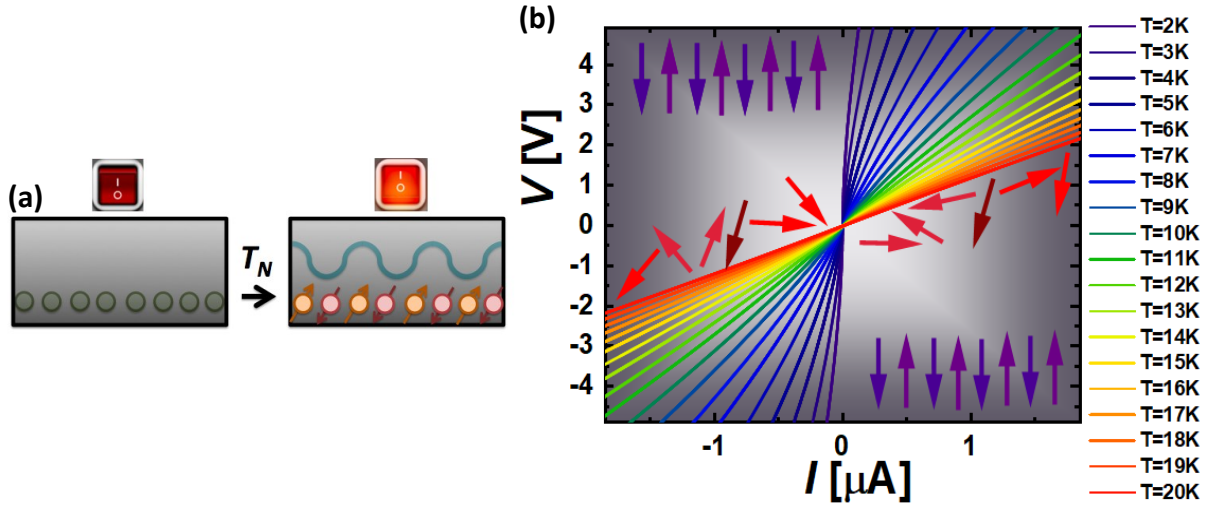

Fig. 20. $EuMn_2P_2$ temperature dependence of 31P NMR spectrum. The line shift, as well as the line broadening both follow the magnetic susceptibility. The broadening implies that the average Mn-P are changing as we lower the temperature implicit to weak Mn ordering present in $EuMn_2P_2$.

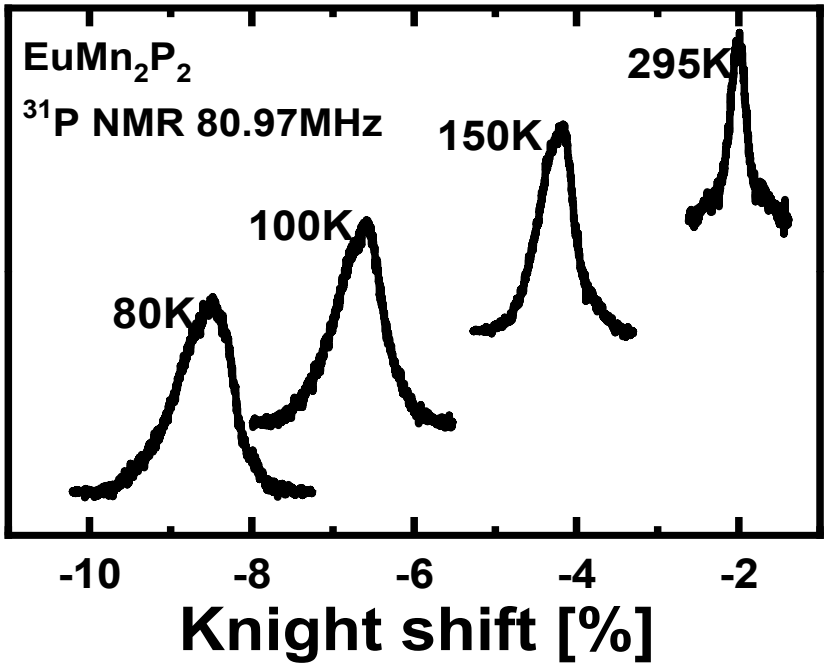

References:

1. A. C. Payne, A. E. Sprauve, M. M. Olmstead, S. M. Kauzlarich, J. Y. Chan, B. A. Reisner, J. W. Lynn, Synthesis, magnetic and electronic properties of single crystals of $EuMn_2P_2$. *Journal of Solid State Chemistry*, **163**, Issue 2 (2002).
2. G.M. Sheldrick, A short history of SHELX, *Acta Cryst. A* **64**, 112-122 (2008).
3. L.J. Farrugia, WinGX suite for small-molecule single-crystal crystallography, *J. Appl. Cryst.* **32**, 837-8 (1999).
4. A.B. Kuzmenko, Kramers-Kronig constrained variational analysis of optical spectra, *Rev. Sci. Inst.* **76**, 083108 (20015).
5. Tari, A. The Specific Heat of Matter at Low Temperatures. (*Imperial College Press*, London, 2003).
6. J. A. Hoffmann, A. Paskin, K. J. Tauer, R. J. Weiss, Physical Contributions to the Heat Capacity of Nickel, *Journal of Physical Chemistry of Solids* **1**, 45, (1956).
7. R.A. Brand, NORMOS, distributed by Wissenschaftliche Elektronik GmbH, Germany.
8. D. B. Henge, M. Hermus, C. F. Litterscheid, N. Wagner, J. Beck, B. Albert, J. Brgoch, Discovery of γ-MnP_4 and the Polymorphism of Manganese Tetraphosphide. *Inorganic Chemistry* **54**, 8761−8768 (2015).
9. S.S. Stoyko, P.E. Blanchard, K.K. Ramachandran, A. Mar, Quaternary rare-earth transition-metal phosphides $REMnCuP_2$ (RE¼ Y, La-Nd, Sm, Gd-Tm, Lu) with $CaAl_2Si_2$-type structure and a polymorph of $LaMnCuP_2$ with $BaCu_2S_2$-type structure, *Journal Solid State Chem.* **269**, 100e106, (2019).
10. Z. Gercsi, K. Hono, K. G. Sandeman Designed metamagnetism in $CoMnGe_{1-x}P_x$. *Physical Review B*, **83** 174403, (2011).
11. S. Kawakatsu, M. Kakihana, M. Nakashima, Y. Amako, A. Nakamura, D. Aoki, T. Takeuchi, H. Harima, M. Hedo, T. Nakama, Y. ŁOnuki, De Haas—van Alphen experiment and fermi surface properties in field-induced ferromagnetic state of MnP, *Journal of Physical Society Japan.* **88**, 044705 (2019).
12. N. S. Sangeetha, S. Pakhira, Q. Ding, L. Krause, H. Lee, V. Smetana, A. Mudring, B. B. Iversen, Y. Furukawa, D. C. Johnston, First-order antiferromagnetic transitions of $SrMn_2P_2$ and $CaMn_2P_2$ single crystals containing corrugated-honeycomb Mn sublattices. *Proceedings of the National Academy of Sciences*, **118** (44) e2108724118 (2021).
13. J. Cedervall, P. Beran, M. Vennström, T. Danielsson, S. Ronneteg, V. Höglin, D. Lindell, O. Eriksson, G. André, Y. Andersson, P. Nordblad, M. Sahlberg, Low temperature magnetostructural transitions in $Mn_3Ni_{20}P_6$. *Journal of Solid State Chemistry*, **237**, 343−348 (2016).
14. F. Hummel, Magnetism and superconductivity in layered manganese and iron pnictides (Doctoral dissertation, lmu 2015).
15. W. Jeitschko, R. Ruhl, Preparation, properties, and structure refinement of the stacking variant 2-MnP_4, *Materials Research Bulletin*, **15**, 1755 (1980).
16. T. Yu, S. Wang, X. Zhang, C. Li, J. Qiao, N. Jia, B. Han, S.-Q. Xia, X. Tao, $MnSiP_2$: A New Mid-IR Ternary Phosphide with Strong SHG Effect and Ultrabroad Transparency Range. *Chemistry of Materials*, **31**, 2010−2018 (2019).
17. T. N. Lamichhane, V. Taufour, M. W. Masters, D. S. Parker, U. S. Kaluarachchi, S. Thimmaiah, S. L. Budko, P. C. Canfield, Discovery of ferromagnetism with large magnetic anisotropy in ZrMnP and HfMnP. *Applied Physics Letters*, **109**, 092402 (2016).

18. C. A. Payne, M. M. Olmstead, S. M. Kauzlarich, D. J. Webb, Structure, magnetism, and magnetoresistance of the compounds $Eu_{14}MnAs_{11}$ and $Eu_{14}MnP_{11}$, *Chemistry of Materials*, **13**, 1398-1406 (2001).
19. S. Rundqvist, X-Ray Investigations of Mn, P., Mn, P, and Ni, P, *Acta Chemica Scandinavica*, **4**, 992 (1962).
20. S.-H. Na, W. Wu, J.-L. Luo, Anisotropy Properties of Mn_2P Single Crystals with AntiferromagneticTransition*, Chinese Physical Letter*, **37**, 087301 (2020).
21. S. L. Brock, J. E. Greendan, S. M. Kauzlarich, Resistivity and Magnetism of AMn_2P_2 (A = Sr, Ba): The Effect of Structure Type on Physical Properties, *Journal of Solid State Chemistry*, **113**, 303 (1994).